Title

Fitting Jet Noise Similarity Spectra to Volcano Infrasound Data

Journal

Earth and Space Science, 8(11)

ISSN

2333-5084

Authors

Gestrich, JE

Fee, D

Matoza, RS

et al.

Publication Date

2021-11-01

DOI

10.1029/2021ea001894

AGU ADVANCING EARTH AND SPACE SCIENCE

Earth and Space Science

RESEARCH ARTICLE
10.1029/2021EA001894

Fitting Jet Noise Similarity Spectra to Volcano Infrasound Data

J. E. Gestrich[1], D. Fee[1], R. S. Matoza[2], J. J. Lyons[3], and M. C. Ruiz[4]

[1]Alaska Volcano Observatory, Geophysical Institute, University of Alaska Fairbanks, Fairbanks, AK, USA, [2]Department of Earth Science and Earth Research Institute, University of California, Santa Barbara, CA, USA, [3]U.S. Geological Survey, Alaska Volcano Observatory, Anchorage, AK, USA, [4]Instituto Geofísico, Escuela Politécnica Nacional, Quito, Ecuador

Abstract Infrasound (low-frequency acoustic waves) has proven useful to detect and characterize subaerial volcanic activity, but understanding the infrasonic source during sustained eruptions is still an area of active research. Preliminary comparison between acoustic eruption spectra and the jet noise similarity spectra suggests that volcanoes can produce an infrasonic form of jet noise from turbulence. The jet noise similarity spectra, empirically derived from audible laboratory jets, consist of two noise sources: large-scale turbulence (LST) and fine-scale turbulence (FST). We fit the similarity spectra quantitatively to eruptions of Mount St. Helens in 2005, Tungurahua in 2006, and Kīlauea in 2018 using nonlinear least squares fitting. By fitting over a wide infrasonic frequency band (0.05–10 Hz) and restricting the peak frequency above 0.15 Hz, we observe a better fit during times of eruption versus non-eruptive background noise. Fitting smaller overlapping frequency bands highlights changes in the fit of LST and FST spectra, which aligns with observed changes in eruption dynamics. Our results indicate that future quantitative spectral fitting of eruption data will help identify changes in eruption source parameters such as velocity, jet diameter, and ash content which are critical for effective hazard monitoring and response.

Plain Language Summary Detecting and quantifying the amount of ash and other material that erupted is important for effective hazard mitigation. One method to observe eruptions is to record low-frequency sound that is produced during the eruption, called volcano infrasound. However, the source of volcano infrasound produced by energetic eruptions is complex. Tam et al. (1996, https://doi.org/10.2514/6.1996-1716) showed that small jets in the laboratory generate sounds with two different but characteristic spectral shapes that are produced by two kinds of turbulence: fine-scale turbulence and large-scale turbulence. Volcanoes produce large jets with complex eruption flows, and here we examine the similarity of their spectral shape compared to laboratory jets using a nonlinear spectral fitting technique. We find that volcanic jets generally produce noise similar to laboratory jets, while times of background noise have a different spectral shape. We also develop a method that shows which frequency bands have the most similar shape to laboratory jets, and find that the jet noise frequencies change as the eruption dynamics evolve. Our results may allow scientists to determine when an eruption is occurring using the infrasound spectral shape, as well as infer volcanic eruption parameters, such as jet velocity and ash content.

Key Points:

- We introduce a technique to quantitatively fit empirical jet noise spectra to volcano infrasound data from different volcanoes
- A decrease in misfit during eruptions suggests that spectral fitting can distinguish between eruption and noise
- Spectral fitting shows jet noise frequencies change as the eruption dynamics evolve

Supporting Information:

Supporting Information may be found in the online version of this article.

Correspondence to:

J. E. Gestrich,
jegestrich@alaska.edu

Citation:

Gestrich, J. E., Fee, D., Matoza, R. S., Lyons, J. J., & Ruiz, M. C. (2021). Fitting jet noise similarity spectra to volcano infrasound data. *Earth and Space Science*, *8*, e2021EA001894. https://doi.org/10.1029/2021EA001894

Received 25 JUN 2021
Accepted 7 OCT 2021

Author Contributions:

Data curation: D. Fee, R. S. Matoza, J. J. Lyons, M. C. Ruiz
Formal analysis: J. E. Gestrich
Funding acquisition: D. Fee
Methodology: J. E. Gestrich, D. Fee, R. S. Matoza, J. J. Lyons
Project Administration: D. Fee
Resources: D. Fee, R. S. Matoza, J. J. Lyons, M. C. Ruiz
Software: J. E. Gestrich
Supervision: D. Fee
Validation: D. Fee
Visualization: J. E. Gestrich
Writing – original draft: J. E. Gestrich
Writing – review & editing: D. Fee, R. S. Matoza, J. J. Lyons, M. C. Ruiz

1. Introduction

The eruption of gas and other material by volcanoes perturbs the surrounding air and generates pressure waves, including acoustic waves. Due to the large dimensions of volcanoes and volcanic events, the associated sounds are usually in a low-frequency band below human audibility, called infrasound. The physical source process generating the infrasonic waves can vary for different eruptions or even within an eruption. An often used analogy was introduced by Woulff and McGetchin (1976) and describes the volcano acoustic source mechanism as a combination of the monopole, dipole, and quadrupole components. However, as pointed out by Matoza et al. (2013), these analogies may be oversimplified for volcanic sources, especially for eruptions with sustained gas and ash jets and limited sampling of the acoustic wavefield.

The term "jet" has been commonly used to describe rapid and sustained gas release from a volcano (Kieffer & Sturtevant, 1984; McKee et al., 2017; Wilson, 1976). A jet is usually associated with the rapid projection of

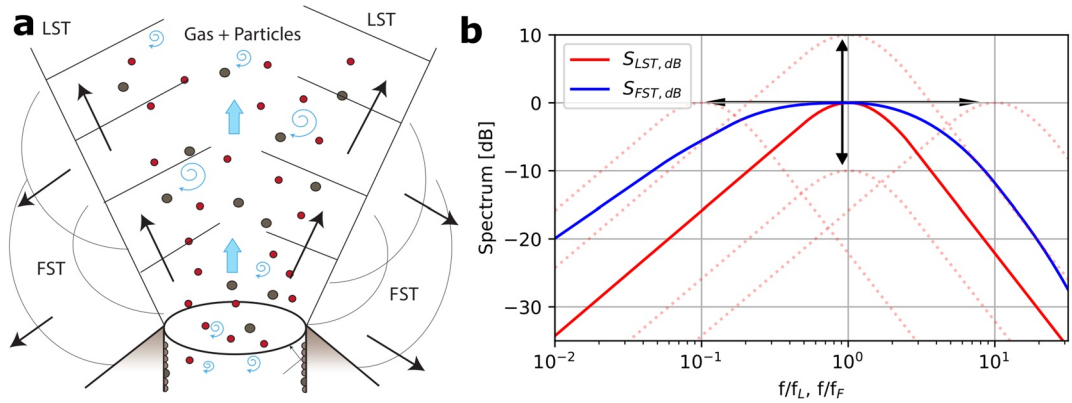

Figure 1. (a) Sketch of the distribution of large-scale turbulence (LST) and fine-scale turbulence (FST) jet noise emanating from a volcano, adapted from Figure 2 in Matoza et al. (2013). The blue arrows show the velocity direction of the erupting gas (blue spirals) and particles (red and brown circles). The black lines and arrows show the pressure wave fronts and radiation direction of LST and FST waves. (b) Similarity spectra for LST (solid red) and FST (solid blue) jet noise normalized with $C_i = 1$. The arrows and dotted red curves show how the spectrum can vary in amplitude (up and down) and peak frequency (left and right) without changing its shape.

a fluid through a nozzle into a steady fluid. When the projected low viscosity fluid is fast and the nozzle is small the fluid becomes turbulent through instabilities in the fluid motion (Oertel, 2004). A typical measure of turbulence is the dimensionless Reynolds number $\mathrm{Re} = uL/\nu$, with u and L being the representative velocity and length scale of the fluid and ν the kinematic viscosity. When the Reynolds number increases the fluid becomes turbulent. Volcanic jet flows (e.g., Figure 1a) have very high Reynolds numbers (e.g., $> 10^{11}$ [Kieffer & Sturtevant, 1984]) and are therefore turbulent.

Geophysical spectra are often compared to modeled spectra to help understand physical source processes. For example, turbulence, particle impacts, and resonance may produce spectral shapes identifiable in volcano seismic and acoustic data (e.g., Ferrick et al., 1982; Gestrich et al., 2020; Julian, 1994; Watson et al., 2019). Quantitative spectral comparison can then be used to identify specific features and parameters useful for understanding eruption dynamics (Watson et al., 2019). Extensive experimental data show that there are two distinct components of jet mixing noise in a sustained jet that contribute to the sound generation (e.g., Tam, 2019, and references therein): large-scale turbulence (LST) and fine-scale turbulence (FST). FST is attributed to fine-scale eddies producing pressure variations and therefore sound. Due to the random and chaotic movement of the eddies, the associated spectrum is very broadband (Figure 1b) and the radiation pattern is nearly isotropic. LST is associated with coherent instability waves that radiate Mach waves (e.g., Tam & Burton, 1984a, 1984b; Tam et al., 1996). These waves form at the outside of the jet stream in a cone-shaped pattern (Figure 1a) and are thought to be generated along the jet boundary, close to the nozzle exit, and move like a "wavy wall" at supersonic speeds (Tam, 2019). The LST sound radiation is highly directional, and the spectrum is narrower than that of FST (Figure 1b). It has been argued that the directionality of the LST noise may be reduced at volcanoes because of strong diffraction at low frequencies and the increase in cone angle for high-temperature jets (Matoza et al., 2009). Sustained Mach wave radiation has been visually interpreted from volcanic eruptions (e.g., Genco et al., 2014; Taddeucci et al., 2014). Some previous studies (Fee et al., 2010; Matoza et al., 2009) noted that the LST appeared to most closely resemble volcanic infrasound data from large eruptions. However, we consider both turbulence models in this work as it has been shown that FST dominates at certain angles from the jet and these angles can be modified by temperature, atmospheric conditions, and topography (e.g., Matoza et al., 2013; Tam et al., 1996; Viswanathan, 2009).

The underlying empirical spectra for LST and FST, called jet noise similarity spectra by Tam et al. (1996), were determined and tested against a large number of audible jet spectra, in fact, the entire jet noise catalog at NASA Langley at that time. These spectra have been extensively used to characterize jet noise from anthropogenic jets (e.g., Harker et al., 2013; Kandula, 2008; Neilsen et al., 2013). Jet flow is considered self-similar, meaning that the same turbulent features are observed for a range of jet operating parameters.

The resultant acoustic spectra are also similar in shape and only vary in amplitude and peak frequency, which is the frequency of the spectrum's maximum amplitude. The application of the similarity spectra to volcanoes, which are many times larger than laboratory jets, indeed shows a similar spectral shape and lower peak frequency f_p (Fee & Matoza, 2013; Fee et al., 2010; Matoza et al., 2009). The comparison of numerical simulations of turbulent eddies to infrasound data is also promising (Cerminara et al., 2016). The lower peak frequency can be explained considering the Strouhal number, a non-dimensional parameter used to describe the oscillating flow. The peak Strouhal number $Str_p = f_p D_j / U_j$, connects the peak frequency with the expanded jet diameter D_j and the jet velocity U_j. Matoza et al. (2009) noted that the volcanic jet diameter is about three orders of magnitude larger than laboratory jets and the recorded peak frequency about three orders of magnitude lower and we assume a similar jet Mach number $Ma = U_j / c$ between volcanoes and experiments of 0.3–1.3 (Genco et al., 2014; Kieffer & Sturtevant, 1984; McKee et al., 2017). Consequently, roughly similar Strouhal numbers have been observed between volcanic eruptions (0.06–1.8; McKee et al., 2017) and experiments (0.2–0.6; e.g., Lighthill, 1954).

The spectral fits by Matoza et al. (2009) and Fee et al. (2010) were preliminary and the applicability of these spectra to volcano acoustic data is still largely qualitative and the effect of volcanic jet complexities on the spectra is poorly understood. Here, we develop a tool to automatically and quantitatively fit the laboratory-derived empirical jet noise similarity spectra from Tam et al. (1996) to volcano infrasound data and evaluate their fit through time and frequency space. A more detailed description of the similarity spectra can be found in Section 2.1. We find that spectra of eruptive signals have a more similar shape to the similarity spectra than spectra during times of non-eruptive background noise. The difference in source and spectral shape between eruption and background noise can be found in Sections 3.4 and 4.2. The fitting of different frequency bands highlights the changes of the frequency spectrum shape during the eruption in Section 4.1. Quantitative fitting can help advance future research on connecting the differences and similarities between the recorded and model spectra to observed dynamics such as particle volume fraction, temperature, velocity, and vent shape. This will help inform the formulation and application of a physical jet noise source model for large, sustained, hazardous eruptions. Furthermore, we discuss if a quantitatively good fit is unique to times of eruption or can also be found in times of background noise.

2. Methods

The goodness of fit between a model and data informs about the validity and applicability of the model. Here we use the similarity spectra equations, empirically derived by Tam et al. (1996), as the model spectra for jet noise. We will use the terms *similarity spectrum* and *model (spectrum)* synonymously throughout the rest of this manuscript but we emphasize that a first principles noise model for jet noise is not complete. Volcano-specific complexities such as particle load, temperature, and vent erosion are not accounted for in the model spectra as they were derived from gas-only jets. The difference between the similarity spectra and eruption spectra might provide insight into the influence of those dynamics on the spectrum. The nonlinearity of the equations requires an appropriate least squares method, and we choose the Gauss-Newton algorithm. The misfit between the spectra is dependent on the choice of frequency bandwidth and optional restriction of the peak frequency to a certain range.

2.1. Similarity Spectra Equations

Tam et al. (1996) introduced Equations 1 and 2 describing the FST (S_{FST}) and LST (S_{LST}) noise spectra. The spectra are designed so that they keep the same shape in any location in the logarithmic frequency and decibel space as indicated by the arrows and dotted red lines in Figure 1b. The decibel levels for the similarity spectra as well as for the power spectra calculated from the recorded data are referenced to a spectral level of $(20\,\mu\mathrm{Pa})^2/\mathrm{Hz}$. The amplitude is dependent on the numerical factors A and B, the ratio between the distance to the nozzle r and the expanded jet diameter D_j. We redefine these variables to C_{LST} and C_{FST} so that we only have one numerical value that defines the amplitude of each spectrum. The functions F and G are each dependent on the peak frequency for LST f_L and FST f_F (shown in Text S1 in Supporting Information S1) and define the characteristic shape of the similarity spectra shown in Figure 1b. This means we can identify four model parameters $C_{\mathrm{LST}}, C_{\mathrm{FST}}, f_L, f_F$, with the first two defining the amplitudes of the model (similarity) spectra and the last two the lateral position in the frequency space. The general description of jet

noise is the sum of Equations 1 and 2: $S = S_{\mathrm{LST}} + S_{\mathrm{FST}}$. When one of the turbulence types has a negligible contribution, the final noise spectrum can be described by Equation 1 or 2. In the following, we will focus on fitting the similarity spectra for LST and FST separately to determine their individual contribution to the overall spectrum.

$$S_{\mathrm{LST}} = \underbrace{A\left(\frac{r}{D_j}\right)^{-2}}_{C_{\mathrm{LST}}} \cdot F\left(\frac{f}{f_L}\right) \tag{1}$$

$$S_{\mathrm{FST}} = \underbrace{B\left(\frac{r}{D_j}\right)^{-2}}_{C_{\mathrm{FST}}} \cdot G\left(\frac{f}{f_F}\right) \tag{2}$$

2.2. Fitting Method

Due to the nonlinearity of Equations 1 and 2, we use a least squares method for nonlinear equations to fit the similarity spectra to the volcano infrasound data. The Gauss-Newton algorithm is specifically designed to solve this problem and has been used in many applications (e.g., Foresee & Hagan, 1997; Kanasewich & Chiu, 1985; Wright & Nocedal, 1999). We use a modified version called the Trust Region Reflective Algorithm. Trust region algorithms have been used in full-waveform inversion (Peng et al., 2017) and reflection tomography (Delbos et al., 2006) and are generally considered stable and fast. Additionally, this method is able to consider bounded parameters which allow us to restrict the parameters, for example, the peak frequency values, to a specific range.

We define the misfit function to be minimized as

$$M = 1/n \sum^{n} (S_{dB,i} - d_i)^2 \tag{3}$$

$$= 1/n \|\vec{S_{dB}} - \vec{d}\|_2^2 \tag{4}$$

$$= MSD \tag{5}$$

which is also the mean squared deviation, MSD, of the difference between the similarity spectrum in decibel, S_{dB}, and the data, d. Both similarity spectrum and data are expressed in decibel scale (dB relative to (20 μPa)^2/Hz (shortened to dB)) and resampled in logarithmic frequency space because the similarity spectra were originally empirically derived in these units (Tam et al., 1996). In the following section we present results for $RMSD = \sqrt{MSD}$, the root-mean-square deviation, which has the same units as the spectra (dB relative to (20 μPa)^2/Hz).

We consider two broad approaches to fit the similarity spectra to the measured spectra. The first one is to fit the models to the whole measured eruption spectrum. This is consistent with the common assumption that the whole spectrum is produced by the sound of turbulence (Tam et al., 1996). The second approach is geared toward illuminating which parts of the measured spectra are best fitted by the models. This method requires the use of multiple frequency bands in which we fit the models to the data. Each method has advantages and disadvantages which we discuss in Section 3.5. As noted above, the shapes of the similarity spectra are constant in the log-frequency and decibel space. Therefore, we describe the width f_w of frequency bands in which we fit the models to the measured spectra in a logarithmic scale: $f^{\max} = f^{\min} \cdot 10^{f_w}$, with $f^{\min}$ and $f^{\max}$ being the frequency band bounds. The values of the peak frequencies f_L and f_F can be restricted to a separate frequency band with bounds $f_p^{\min}$ and $f_p^{\max}$. We define overlapping frequency bands in which the similarity spectra are fit to the data and calculate corresponding $RMSD$ values. A detailed description of the method can be found in Text S3 and Figure S1 in Supporting Information S1. We refer to the result as a *misfit spectrum* as shown in Figures 2a–2d. To determine which of the two models, LST and FST, better fit the data over time and frequency we subtract the LST misfit spectrum from the FST misfit spectrum and call this a *misfit difference spectrogram* as shown in Figure 2e. Since this only shows

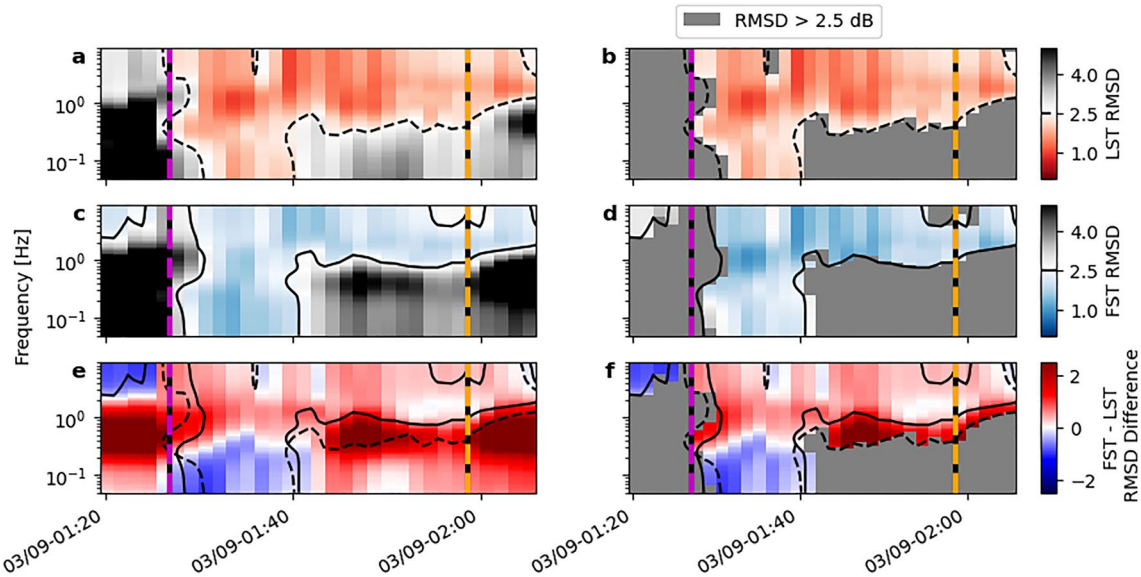

Figure 2. Misfit spectrogram example for the MSH eruption. Large-scale turbulence (LST) misfit spectrogram (a) with outlined $RMSD$ of 2.5 dB in dashed black lines which is then masked in (b) for all $RMSD$s above 2.5 dB. The same is shown for the fine-scale turbulence (FST) model in (c and d). Panel (e) shows the difference between (c and a) with the same outlines as above and (f) shows the same as (e) but masked if both, LST and FST, show higher $RMSD$s than 2.5 dB. The pink-black dashed line marks the start and the orange-black dashed line the end of the eruption.

the differenced $RMSD$ values we mask out times and frequencies that have an $RMSD$ above a certain threshold as shown in Figures 2b, 2d, and 2f. The process is described more fully in Text S3 in Supporting Information S1. The misfit spectrograms for the eruptions of Tungurahua and Kīlauea are shown in Figures S2 and S3 in Supporting Information S1 and the misfit difference spectrograms for all eruptions are also shown in Figures 3d, 4d, 5d1, and 5d2.

3. Data

To explore the method and fit between similarity spectra and eruption signals, we use infrasound data from eruptions at three different volcanoes: Mount St. Helens (MSH), USA; Tungurahua, Ecuador; and Kīlauea, USA. Eruptions of the first two volcanoes have been qualitatively compared to jet noise previously (i.e., Fee & Matoza, 2013; Fee et al., 2010; Matoza et al., 2009). Here, we expand the analysis to include quantitative comparisons to get a better understanding of the applicability of the similarity spectra. Data from these volcanoes have a variety of spectral features and eruption characteristics, and the Kīlauea data were notable in that audible reports of jetting were common. All times are reported in UTC.

The data from each eruption was recorded on an array of microphones. An array consists of multiple sensors located in relative proximity, here between 30 and 100 m. Least squares array processing methods were used to determine the sound back-azimuth and velocity across the arrays (Bishop et al., 2020; Olson & Szuberla, 2005). We stack the time-shifted signals, called delay-and-sum beamforming, to improve the signal-to-noise ratio (SNR). We do not perform any further array analysis to ensure our fitting method is usable for single sensor analysis. We use Welch's method to calculate the power spectrum from the beamformed waveform, which takes the average of overlapping data windows that have been Fourier transformed (Welch, 1977). Here we generally compute power spectra for a 10 min segment, using 1 min Hann windows with 30 s overlap. The MSH eruption is an exception where we use a 5 min segment because the most energetic part of the eruption is of relatively short duration. To assure that we capture significant changes in the spectra the power spectrum time segments overlap by 70%. The power spectra are resampled with logarithmic spacing and a rolling median filter is applied with a window width of $f \cdot (10^{1/8} - 1)$.

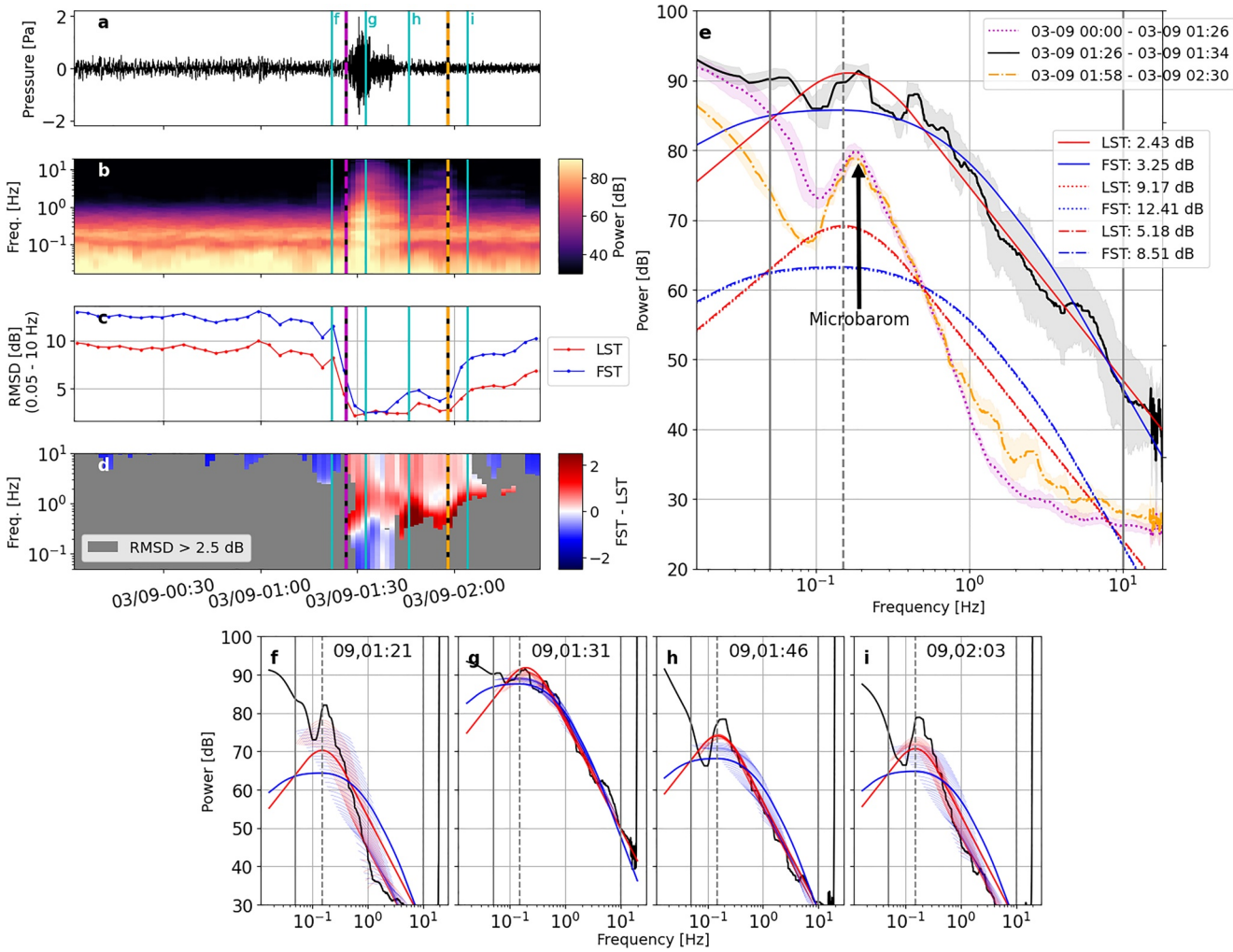

Figure 3. March 2005 Mount St. Helens eruption infrasound and spectral fitting showing the (a) infrasound waveform filtered above 0.01 Hz, (b) spectrogram, (c) overall $RMSD$ for large-scale turbulence (LST) (red) and fine-scale turbulence (FST) (blue) between 0.05 and 10 Hz and (d) misfit difference spectrogram plot showing times and frequencies of low $RMSD$ for LST (red) and FST (blue). The pink-black dashed lines show the beginning and the orange-black dashed lines at the end of the eruption and the solid light blue lines show the timing of the power spectra shown in (f–i). In (e), we show the median power spectrum for the time of the eruption (solid black) and background noise before (dotted pink) and after (dashed orange) with shaded areas showing the median absolute deviation for the time periods specified in the legend. The median solutions for the LST (red) and FST (blue) with their respective $RMSD$s are shown in the legend. In (f–i), power spectra for the times marked in light blue in (a–d) and labeled in the top of each plot are shown in black, as well as the overall model solutions with solid red and blue lines for LST and FST with shown $RMSD$ in (c). The solutions for the smaller frequency bands that were calculated for the misfit spectrogram in (d) are plotted as semi-transparent lines. In (e–i), the dark gray solid lines show the 0.05 and 10 Hz frequency limits and the dark gray dashed line 0.15 Hz which is the lower bound of the peak frequency restriction. Panel (c) shows a clear drop in $RMSD$ at the start of the eruption which indicates that the eruption spectrum is more likely to be produced by jet turbulence than the background noise. The background noise is dominated by the microbarom peak shown in (e). The initial minutes of the high-velocity gas thrust are very well fit by the similarity spectra.

3.1. Mount St. Helens

During the MSH eruptive period of 2004–2008, an infrasound array was deployed approximately 13.4 km from the active vent. The array consisted of four MB2000 microbarometers with a flat response between 0.01 and 17 Hz. We remove the instrument response from the data. Details about the deployment are described in Matoza et al. (2007). The eruption we analyze here occurred on March 9, 2005, and is the most energetic eruption of that eruptive period. This phreatic eruption lasted 30–50 min with an initial 7 min long energetic gas thrust phase that quickly decreases in amplitude (Matoza et al., 2009). The following minutes of signal have a back-azimuth pointing to the volcano but the amplitude is very low and the spectral shape

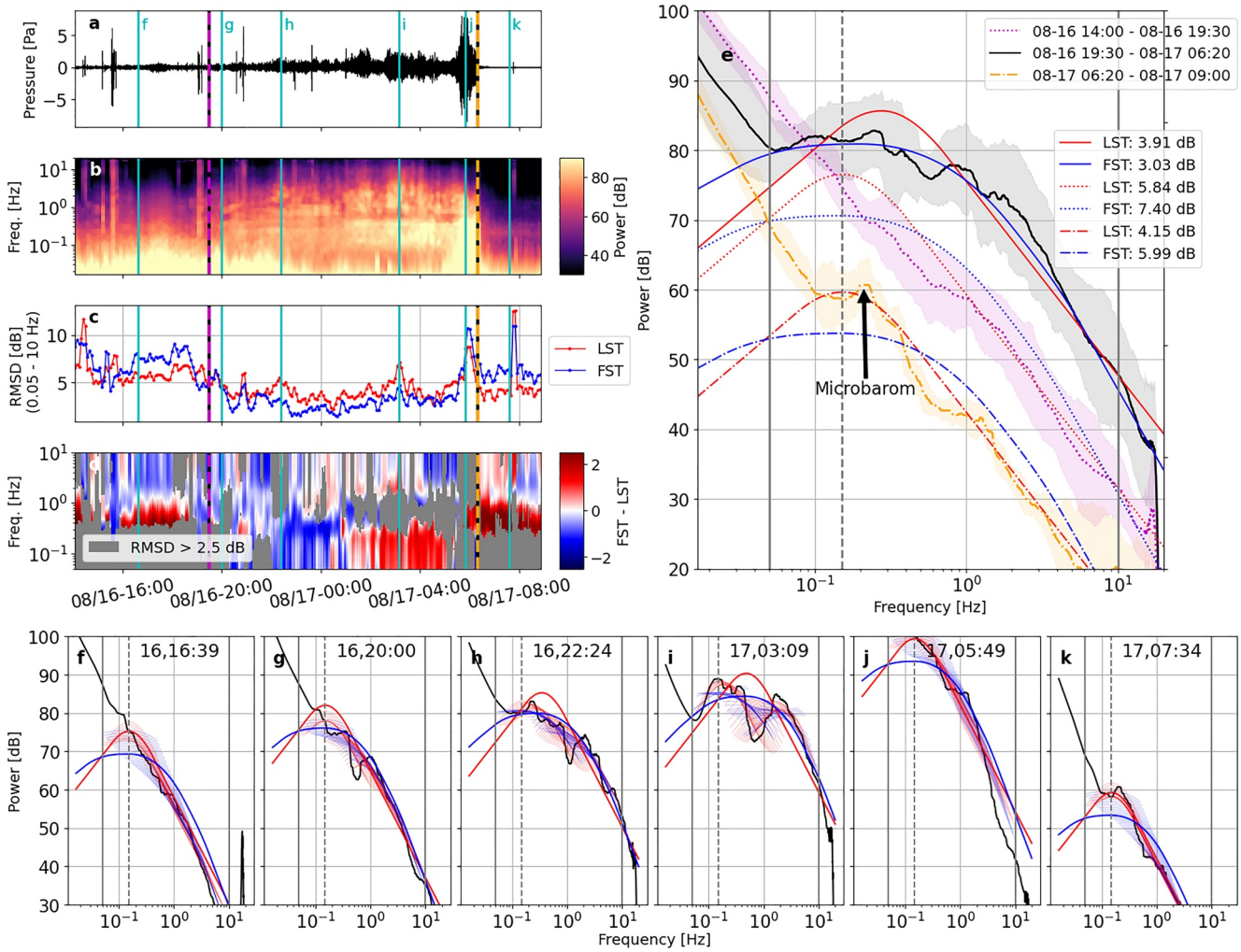

Figure 4. August 2006 Tungurahua eruption infrasound and spectral fitting. The figure layout is the same as Figure 3. In (c), we see a drop of $RMSD$ at the start of the eruption and in (d) there is high variability in the frequency bands that are fit best by large-scale turbulence (LST) and others by fine-scale turbulence (FST) through time. This is due to the high variability in the eruption power spectrum shape as shown in (g–i). The last paroxysmal hour of the eruption shown in (j) has a different shape than the similarity spectra.

only deviates slightly from background noise for frequencies >0.8 Hz. The waveform and spectrogram of the analyzed time period are shown in Figures 3a and 3b and power spectra for the labeled times are shown in Figures 3e–3i.

3.2. Tungurahua

Infrasound arrays deployed in the vicinity of Tungurahua (Garcés et al., 2008) recorded a variety of eruptions between 2006 and 2008: sub-Plinian (July 2006), Vulcanian (February 2008), and a Plinian eruption in August 2006. We use data recorded on the closest array, RIOE, approximately 36.7 km from the active vent, which consisted of four Chaparral 2.2a microphones with a flat response between 0.1 and 200 Hz sampled at 40 Hz. We remove the instrument response from the data and note that some of the analyzed data are below the lower −3 dB cutoff. We refer to Fee et al. (2010) for further details on the deployment and the eruption early warning system they developed.

The Plinian eruption on August 16–17 produced ash reaching heights of 24 km above sea level (ASL) and lasted ~11 h. The eruption emerges gradually at 19:30 and changes from being ash-poor to lava fountaining with ash-rich jetting to highly energetic explosions and a substantial increase in plume height up to

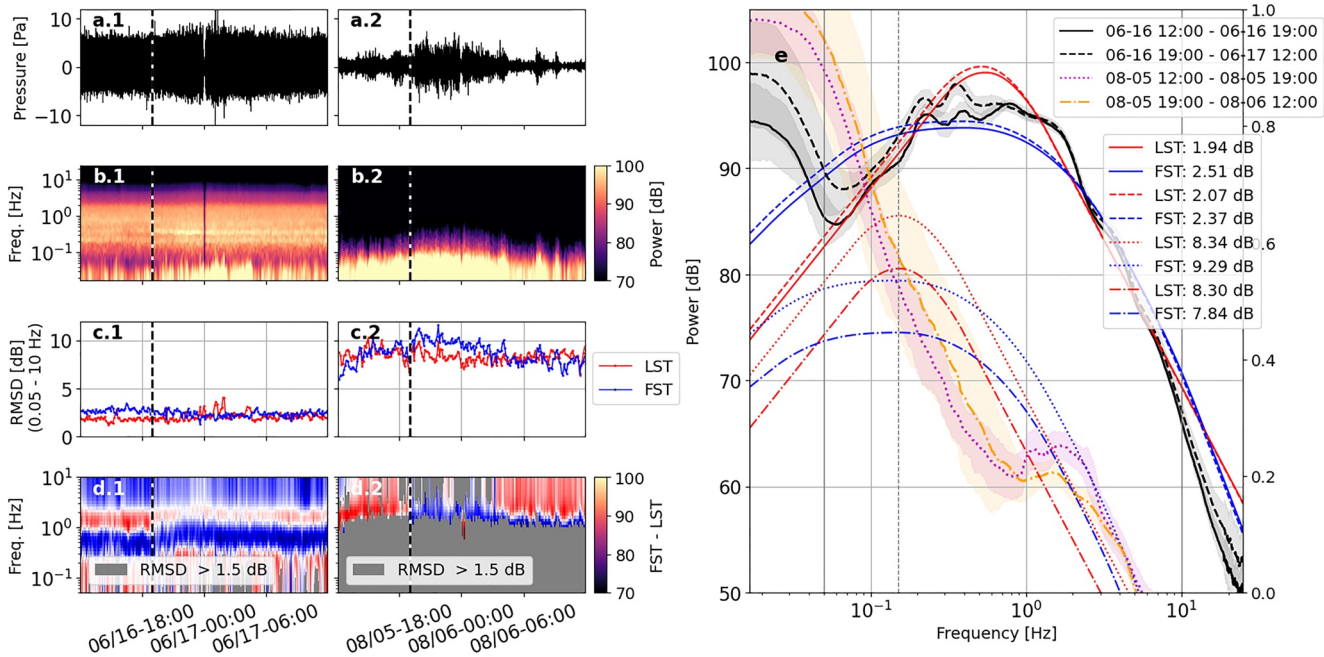

Figure 5. June 2018 Kīlauea's fissure eight, Ahu'ailā'au, eruption infrasound. The figure layout is the same as in Figure 3 and 4 with some minor changes: Here, (a.1–d.1) show one day of data during the eruption (June 16/17), with a ~20 min data gap around 00:00, and (a.2–d.2) show one day of data after the eruption (August 5/6). The black and white dashed line in (a.1–d.1) shows the timing (19:00) of a change in the spectrogram and fitting mentioned in the text (not eruption start and end as in Figures 3 and 4). In (e), we show the median power spectrum before (solid black) and after (dashed black) the change. In (a.2)–(d.2), the same time of day (19:00) is marked with a black and white dashed line and the median power spectrum before the marked line is shown in (e) with a dotted pink line and the median power spectrum after is shown as a dot-dashed orange line. The blue and red lines in the same subplot are the median solutions for large-scale turbulence (LST) and fine-scale turbulence (FST) for the same times with the linestyle (dotted, dashed, etc.) corresponding to the style of the shown median power spectra. We can see that the LST similarity spectrum generally fits the data very well during the eruption (black lines), especially on the flanks. The FST similarity spectrum fits better at the peak of the eruption spectrum. The increase of the spectral power at approximately 0.35 Hz results in a decrease of $RMSD$ for the FST spectrum. The background noise power spectra (pink and orange) are less well fitted by the LST and FST spectra.

17.5 km between 22:00 (August 16) and 5:30 UTC (August 17). The following paroxysmal phase lasts for one hour with an ash column reaching up to 24 km height and a 6 km tall lava fountain (Fee et al., 2010; Hall et al., 2013). The associated waveform and spectrogram are shown in Figures 4a and 4b and power spectra for certain times in Figures 4e–4k.

3.3. Kīlauea 2018

The eruption of fissure 8, Ahu'ailā'au, in Kīlauea's lower East Rift Zone (LERZ) in 2018 lasted from May 27 to August 4. The eruption at this fissure was preceded by an inflation signal at Pu'u 'Ō'ō and rise of its lava lake level until the crater floor collapsed on April 30. Increases in seismicity propagated eastward and coincided with deformation, indicating magma movement that erupted at the first fissure in the LERZ on May 3 and focused on Ahu'ailā'au on May 27–28 (Neal et al., 2019). The fissure produced a lava fountain of up to 80 m height and jet-like noises were consistently reported by field teams and the public. The fountain eventually decreased in height but continued to produce a high flux of lava. A 4-element campaign infrasound array was installed about 500 m NW of the fissure and operated between June 4 and August 17. The deployed Chaparral 60 UHP infrasound sensors have a flat response between 0.03 and 200 Hz at a 400 Hz sampling rate. Data from this infrasound array has been used to characterize cyclic effusion between July 14 and 21 (Patrick et al., 2019) and associated back-azimuth changes tracking the infrasonic source between the fountain location and the spillway during surges (Lyons et al., 2021). Here, we analyze 24 h of eruption data from June 16 to 17 and compare it to post-eruptive signal from August 5 to 6 shown in Figure 5.

3.4. Eruption Spectrum

The infrasound power spectrum during an eruption has a different shape than during times of background noise (Figures 3e–5e). Despite the different shapes between the eruption and background noise, the power generally decreases similarly as a function of frequency ($\sim 10\log_{10}(f^{-2.7})$). This is likely due to the fact that infrasound background noise is typically composed of turbulence-generated wind (e.g., Hedlin et al., 2012; Raspet & Webster, 2015). An exception is the microbarom peak, which is an acoustic signal produced by energetic ocean waves (e.g., Donn & Naini, 1973; Waxler & Gilbert, 2006), and whose appearance and shape is dependent on the atmospheric conditions for propagation and source (e.g., Bowman & Lees, 2017; Hupe et al., 2019). The microbarom is typically focused between 0.1 and 0.5 Hz with its peak around 0.2 Hz (Bowman et al., 2005), which is a similar frequency band as the eruptions shown in Figures 3e and 4e. The microbarom shows a more rapid decrease in power after the main peak, whereas the eruption signal is more broadband. More details on spectral shape comparisons are discussed in Section 4.2. For the eruptions examined here, the deviation from background noise begins for frequencies above ~0.05 Hz. They generally consist of a distinct increase in power up to a maximum at 0.2–0.3 Hz, which we call peak frequency (Figures 3e–5e). This distinctive deviation from background noise up to a peak frequency is one of the main assumptions we will make when choosing parameters for fitting the similarity spectra to the measured data. All eruption data examined here have been confirmed to originate from the direction of the volcano using array processing. They show similarities in their frequency band, peak frequency, and elevated amplitude above background noise, but differ in actual shape and frequency roll-off. This suggests that the fit with the similarity spectra will differ too.

3.5. Importance of Frequency Bandwidth

The choice of the frequency bandwidth and restriction of variability in peak frequency depends on the analysis target and has notable effects on the misfit. In our fitting analysis, we attempt to balance three primary objectives: (a) fitting the whole spectrum, (b) illuminating which part of the spectrum fits the models, and (c) distinguishing background noise from eruptions. We discuss the trade-offs in the following sections.

Generally speaking, wider frequency bands assure that the whole similarity spectrum fits the measured spectrum. This assumes that the acoustic signal is produced by one turbulence source. We choose the frequency band of 0.05–10 Hz to span the whole frequency space of eruption signal. Although this lower bound is below the −3 dB corner at 0.1 Hz of the RIOE array microphone instrument response, the vast majority of the analyzed frequency band is still in the flat portion of the instrument response. We assume that the turbulence spectrum produced by the eruption peaks within this frequency band and deviates from the background noise by a power increase. This means we can restrict the peak frequencies f_L and f_F within a fraction of this frequency band. This restriction avoids low $RMSD$ due to background noise that has a similar roll-off slope. Here, we use 0.15–10 Hz to restrict the peak frequencies, with 0.15 Hz being just below the peak frequencies of the measured spectra for the three chosen eruptions and at similar eruptions worldwide (e.g., Dabrowa et al., 2011; Fee & Matoza, 2013). Fitting the spectrum as described is consistent with the assumption that the whole eruption spectrum is being produced by turbulence. However, the measured spectra are variable and do not necessarily fit the model spectra perfectly because of irregularities in the measured spectrum. This can be observed during all three eruptions shown in Figures 3f–3i, 4f–4k, and 5e. For example, during the eruption of Kīlauea, the power spectrum displayed in Figure 5e shows a good fit with the LST spectrum on the waxing and waning sides of the power spectrum. However, the peak of the measured spectrum is flatter than the model spectrum.

In contrast, smaller, overlapping frequency bands provide more resolution on how the fitting varies as a function of frequency. Volcano acoustic spectra are occasionally composed of multiple sources and can be altered by atmospheric effects, topography, and potentially other eruption parameters such as temperature and particle volume fraction. Fitting narrower frequency bands to the eruption spectrum allow us to analyze which frequencies are best fit by the similarity spectra. However, when the frequency band becomes too small, we run into the problem that we are not fitting the spectrum's overall shape but small scale irregularities. In our analysis, we choose a frequency bandwidth of $f_w = 1$ with $f_{\max} = f_{\min} \cdot 10^{f_w}$. This width is wide enough to cover 43% of the frequency band that we consider contains eruption signal. Here, we restrict the peak frequency in the same frequency band as for the other analysis, between 0.15 and 10 Hz based on the

same assumption that we are targeting a turbulence spectrum that peaks in this frequency band. Note that fitting a smaller frequency band often leads to a lower $RMSD$. Therefore we compare the $RMSD$ values only to values derived by the same method or in a relative context, such as when a value decreases or rises in both methods.

4. Results and Discussion

In this section, we investigate how well the similarity spectra fit the various eruptions. We examine the general fit during the eruption and compare the fit between LST or FST and the eruptions, as well as the difference between eruption and background noise. Furthermore, we connect phases in eruption dynamics with changes in the misfit difference spectrogram.

In the following sections, we will refer to Figures 3–5 which show the results for the Mount St. Helens, Tungurahua, and Kīlauea eruptions, respectively. They are divided into multiple subfigures showing (a) the beamformed infrasound waveform, (b) the spectrogram, (c) the overall $RMSD$ value for the frequency band of 0.05–10 Hz, and (d) the misfit difference spectrogram. The median power spectra for eruption and background noise, as well as the median model solution for the respective times, are shown in (e). The last subfigures starting with (f) show the power spectra of the times that are indicated with light blue vertical lines in subfigures (a–d). The solid red and blue lines show the solutions for the large (0.05–10 Hz) frequency band and the thinner lighter lines show the solutions for the narrow overlapping frequency bands used for the misfit spectrogram.

4.1. Model Fit During Eruptions

Here, we investigate how changes in the measured spectrum reflect in the fitting and $RMSD$ of the model spectra, focusing now on the times during the active eruptions between the pinkblack and orange-black dashed lines in subfigures (a–d) in Figures 3 and 4 for the MSH and Tungurahua and all of subfigures (a.1–d.1) of the Kīlauea eruption in Figure 5.

4.1.1. Mount St. Helens

Starting with the MSH eruption we observe a high amplitude broadband spectrum in the first minutes of the eruption, which was inferred to be a high-velocity gas-thrust phase (Matoza et al., 2007). The spectrum peaks at ~0.2 Hz and has a second smaller peak at ~0.45 Hz (Figure 3g). After this initial signal, the amplitude decreases and the spectrum only slightly differs from the background noise spectrum (Figure 3h compared Figure 3i) with a low SNR.

During the initial eruption signal, the fitting of both LST and FST similarity spectra show very low $RMSD$s of around 2.5 dB in the fitting of the 0.05–10 Hz frequency band (Figure 3c). As the eruption progresses the $RMSD$ fluctuates slightly but generally stays low (<5 dB). However, this does not tell us what is changing in the measured spectrum that leads to the fluctuations. Here, the misfit difference spectrogram becomes useful. In the beginning of the eruption, we observe low $RMSD$s for both LST and FST over the whole frequency range of < 2.5 dB. They both only differ marginally with FST having a slightly lower $RMSD$ for frequencies below 0.3 Hz and higher $RMSD$ above 0.3 Hz. Comparing this observation to the 01:31 power spectrum shown in Figure 3g, we observe multiple local minima and maxima between 0.05 and 0.3 Hz. This leads to no notable increase or decrease in overall amplitude, which is well fitted by the very broad peak of the FST similarity spectrum. Above 0.3 Hz, the power fall-off has the same slope as the LST model. After the initial gas thrust phase, ~15 min into the eruption, the misfit difference spectrogram shows relatively high $RMSD$ of above 2.5 dB for frequencies below 0.3 Hz for both similarity spectra (gray color in Figure 2 and in Figure 3d). As previously noted, the spectrum at this point in the eruption deviates only a little from the background with slightly elevated power above 0.3 Hz and a power decrease that is very similar to the LST spectrum (Figure 3h). This suggests the acoustic power produced by the eruption has decreased and is masked by the microbarom at lower frequencies but still dominates for higher frequencies. During that time the eruption was described as ongoing but less intense (Matoza et al., 2007). The median $RMSD$ for the time of the gas thrust phase is lower for the LST model than the FST model for the chosen frequency band of 0.05–10 Hz (Figure 3e), which is consistent with the qualitative assessment by Matoza et al. (2009).

Figures S4 and S5 in Supporting Information S1 compare the $RMSD$ fitting using each sensor of the array separately. Similar results are obtained for each sensor, demonstrating the applicability of the method to single sensor analysis.

4.1.2. Tungurahua

The eruption of Tungurahua in August 2006 is the most complex eruption we analyze and shows the greatest variability in the misfit plots (Figure 4). The eruption begins with a gradual emergence of a broadband signal with slightly elevated power above 0.15 Hz and a local minimum (or "notch") at 0.5 Hz (Matoza et al., 2009), with a difference of ~11 dB to the peak (Figures 4b and 4g). The amplitudes above 0.15 Hz increase and the location of the "notch" moves to higher frequencies (~1 Hz). After 01:00, the amplitude increases substantially by ca 8 dB and the "notch" becomes wider, more pronounced, and shifts to ~0.7 Hz. The spectrum is now deviating from background above ~0.05 Hz. The last hour of the eruption, the paroxysmal phase, has a very different spectrum with elevated power throughout the whole frequency space with no specific peak but rather a constant decrease in power for increasing frequencies (Fee et al., 2010; Matoza et al., 2009). The highest amplitudes during this period are observed well below the flat response cutoff <0.1 Hz. During the eruption (19:30–06:20), the overall $RMSD$ between 0.05 and 10 Hz is <5 dB and generally shows slight fluctuations except for a substantial increase during the last hour of the eruption (Figure 4c). However, looking at the misfit difference spectrogram plot in Figure 4d we see much more variability and can roughly divide the eruption into four parts. Note that the four parts described here are picked based on the acoustic signal and are slightly different from the phases picked in Hall et al. (2013) that follow more closely seismic observations. Between 19:30 and 22:00, the $RMSD$ for both LST and FST is above 2.5 dB for frequencies below 0.3 Hz (Figure 4d and Figure S2 in Supporting Information S1) and lower $RMSD$s for higher frequencies. The power spectrum at 21:15 in Figure 4g shows an increase in power above 0.2 Hz compared to the background noise spectrum before (Figure 4f) and fits the FST well. During this time, steam-rich and ash-poor emissions were described that became more ash-rich after 20:15 UTC (Fee et al., 2010; Hall et al., 2013). The next period between 22:00 and 01:00 shows consistently lower $RMSD$s for the FST model (<1.5 dB) than the LST model (>2 dB) for frequencies below 0.8 Hz (Figure 4d). The power spectrum at 22:24 (Figure 4h) shows very good agreement with the FST spectrum for almost the entire frequency band. This period was also described as highly energetic strombolian with an accompanying 100–200 m high lava fountain and small pyroclastic density currents (PDCs) (Fee et al., 2010; Hall et al., 2013). The third phase between 01:00 and 05:20 shows a substantial change in the misfit difference spectrogram plot with high $RMSD$s above 2.5 dB for both similarity spectra around 0.8 Hz which is visible as a gray band in Figure 4d. This is the signature of the developing "notch" in the spectrum shown in the 03:09 time slice that is bound by two local maxima with steep flanks and small peak area which leads to a better fit of the LST spectrum. The accompanying eruptive activity started with an observed lava fountain 800 m above the crater rim (Hall et al., 2013) and a sudden increase in plume height (Steffke et al., 2010). The lava fountain grew reaching 1.5 km throughout this phase in addition to numerous PDCs and an ash plume increasing in width, length, and height up to 17.5 km (Fee et al., 2010; Hall et al., 2013). It was also described in Hall et al. (2013) as highly energetic strombolian activity. The last hour of the eruption, referred to as the paroxysmal phase in Fee et al. (2010), has a very different shape than the eruption before and resembles the background noise spectra before and after the eruption with a strictly negative slope, with the difference that the eruption signal has much higher amplitude (Figure 4j). The fitting of the similarity spectra during this time shows very high $RMSD$s of 5–10 dB in Figure 4c and > 2.5 dB in Figure 4d. The peak frequency is likely well below what is resolvable by the deployed instruments (Fee et al., 2010). During this time a lava fountain of 6 km height and an ash plume up to 24 km were observed with many PDCs and substantial ash fall (Fee et al., 2010; Hall et al., 2013). The median power spectrum for the hours before the paroxysmal phase (Figure 4e), generally shows a better fit with the FST than the LST. This is different from the analysis presented in Matoza et al. (2009) which states that the LST matches the measured spectrum better while mentioning that the "notch" and the roll-off for higher frequency does not fit the LST very well. In our analysis, the "notch" and associated two local maxima lead to a generally flat peak and the roll-off is best fit by the FST (Figure 4e). Matoza et al. (2009) speculated that the jet's turbulence noise and its interaction with the crater walls, could produce separate peaks and the "notch" may be the space between them, whereas Fee et al. (2010) attributes one of the peaks to PDCs observed in infrared camera imagery.

4.1.3. Kīlauea

The eruption of Kīlauea's fissure 8, Ahu'ailā'au, produced very stable infrasonic spectra until mid-July that resembles jet noise, suggesting a very consistent jet-like source mechanism throughout the eruption. Figures 5a1–5d1 and 5e show one day of acoustic data from the Kīlauea eruption on June 16, 2018, with a ~20 min data gap around 00:00. Diurnal winds contribute to a general increase in amplitudes at very low frequencies (<0.1 Hz) peaking between 21:00 and 00:00 (Fee & Garcés, 2007) and shown in Figures 5a2–5b2. However, the eruption signal dominates for frequencies above 0.1 Hz where no diurnal variations are observed. Even though the eruption spectra are very stable we note some slight changes, such as the increase in power at 0.35 Hz after 19:00 (Figures 5b1 and 5e). The $RMSD$ throughout the 24 h in Figure 5c1 is <3 dB, and even lower for other portions of the eruption. We consider this misfit very low, even compared to the eruptions of MSH and Tungurahua that have $RMSD$s <5 dB. We note a change in the overall $RMSD$ after the amplitude increases around 0.35 Hz at approximately 19:00 for the fitting in the 0.05–10 Hz band (Figure 5c1). Before 19:00, we observe a lower $RMSD$ for the LST model <2 dB compared to the FST model with an $RMSD$ >2.5 dB, which then changes to a more similar $RMSD$ value of the two models of around 2.5 dB. We see a striped pattern in the misfit difference spectrogram (Figure 5d1) throughout the whole 24 h, indicating a lower $RMSD$ for the LST model at <0.3 Hz, then a band of low $RMSD$ for the FST model between 0.3 and 1 Hz and then again lower $RMSD$ for the LST model just above 1 Hz. Although this is true for the whole day the intensity changes and the red band just above 1 Hz gets lighter, which indicates that LST and FST models have a more similar $RMSD$ at that frequency. In Figure 5e, we show the median power spectrum before 19:00 with a solid black line and after with a dashed black line. The flanks and width of the LST similarity spectra have a very similar slope to the measured power spectrum which explains the low $RMSD$s below 0.3 Hz and above 1 Hz. Between these frequencies, the measured spectrum is much flatter than the LST similarity spectrum and is better fit by the broad FST similarity spectrum. We can see a clear change in the measured power spectrum with an increase in power around 0.35 Hz and a decrease at ca, 1 Hz after 19:00. This leads to a generally flatter peak region which is even more similar to the FST model and an overall decrease in $RMSD$ for the FST model (Figures 5c1–5e). Generally, the LST shows a lower $RMSD$ value than the FST (Figure 5e). Fully connecting the spectral changes to the physical source or eruption dynamics at Kīlauea are beyond the scope of this manuscript and a topic of future research. The generally better fit of the LST and FST spectra to the Kīlauea eruption spectrum in comparison to Tungurahua and MSH could also be related to the much shorter distance between the source of the jetting and the microphones. The influence of distance and connected influences like atmospheric conditions and topography on the jet noise spectrum are not discussed in this study.

To summarize, during times of eruption the measured spectrum can vary widely, therefore producing considerable changes in the fit between the data and similarity spectra. Fitting within one large frequency band provides a general overview on the fitting and the fluctuations in $RMSD$, but does not show which frequencies the model spectra are fitting better or worse with time. The misfit difference spectrogram provides resolution in both frequency and time. Generally, all three eruptions show good fits with the similarity spectra. However, the time, frequency band, and averaging method have an influence on the $RMSD$ value.

4.2. Eruption Versus Background Noise

The distinction between times of eruption versus background noise by the fitting of the similarity spectra highly depends on the shape of both the background noise and eruption spectrum. The more dissimilar the eruption spectrum is from the turbulence similarity spectra the more difficult it is to tell them apart by simply looking at the misfit spectrograms and differences. Below we discuss a few examples where the similarity spectra fitting identifies eruption signals well, and one example where the results are ambiguous.

The MSH eruption shows the most obvious change in the $RMSD$ between times of background noise and times of eruption in Figures 3c and 3d, which was also was noted in Matoza et al. (2009). The $RMSD$ during the eruption is below 5 dB while during background noise is above 8 dB. Figures 3e–3i show that during times of background noise there is a clear microbarom peak that has a very different shape in both peak region and fall-off slope than the similarity spectra. However, during the eruption, especially the first minutes of jetting, the power spectrum's shape is very similar to the models, especially LST around the peak

region. This is a good example of how a very poor fit during times of background noise and a very good fit during the eruption results in a large difference in the $RMSD$.

The difference between times of background noise and eruption is harder to identify for the August 2006 Tungurahua eruption. At the beginning of the eruption at 19:30, the $RMSD$ decrease is very apparent in Figure 4c, dropping from >5 dB to <5 dB. Before the eruption start at 19:30 the misfit difference spectrogram in Figure 4d shows that there is high $RMSD$ above 2.5 dB for frequencies below 0.3 Hz. This is a reflection of the measured background noise spectrum having a negative slope between 0.05 and 0.15 Hz and the model spectra a positive slope with the peak frequency being ≥0.15 Hz. For frequencies above 0.15 Hz, the $RMSD$ is below 2.5 dB, which is due to the similar slope angle between the model and the measured power spectrum (Figure 4f). The last hour of the eruption (05:20–06:20) has a very different spectral shape with a strictly negative slope and high amplitudes down to very low frequencies (Figure 4j) as opposed to the spectral shape in the hours before that was defined by an increase in amplitude that deviates from the background noise and peaks around 0.2 Hz. This change in the last hour was noted (e.g., Fee et al., 2010; Matoza et al., 2009) and is also reflected by a high $RMSD$ for that time (Figures 4c and 4d). There was no substantial increase in $RMSD$ between the last hour of eruptive activity and the post-eruptive noise. Smaller explosions were reported after the main event that might contribute to persistent low energy jet noise that is still reflected in relatively low $RMSD$ values. However, looking at the whole eruptive sequence the $RMSD$ before and after the eruption is generally higher than during the eruption, especially for the FST model.

As previously discussed in Section 4.1 the fitting between the similarity spectra and the eruption spectrum during the Ahu'ailā'au eruption of Kīlauea volcano is very good. We now compare this to one day of non-eruptive background noise on August 5, 2018, as shown in Figures 5a2–5e. The fitting between 0.05 and 10 Hz in Figure 5c2 shows much higher $RMSD$ values of >8 dB compared to during the eruption when they are roughly 2–3 dB (Figure 5c1). The misfit difference spectrogram (Figure 5d2) shows high $RMSD$s below 1 Hz which is, similar to the Tungurahua example, connected to the negative slope of the spectrum and the positive slope of the similarity spectra below 0.15 Hz. At ∼2 Hz, we observe an increase in amplitude which has a better fit to the LST spectrum in the beginning of the misfit difference spectrogram and decreases in amplitude throughout that day. This leads to a better fit with the FST spectrum. Overall the power spectrum during the Ahu'ailā'au eruption is much better fit by the LST and FST similarity spectra than during non-eruptive background noise, which is consistent with the observations during the MSH and Tungurahua eruptions described above, and further suggests Ahu'ailā'au emitted jet noise.

5. Conclusion

Evaluating the fit of a model spectrum to a measured spectrum is key in assessing the model's validity and determining source parameters. Here, we developed a tool to quantitatively fit the empirical jet noise similarity spectra, originally developed for audible laboratory jets by Tam et al. (1996), to volcano infrasound data. The tool uses a nonlinear fitting algorithm to fit data in a given frequency band with a restricted peak frequency range and calculates the $RMSD$ between the data and model spectra. We apply this tool to volcano acoustic data from notable eruptions at three volcanoes that produced volcanic jet noise. The bandwidth is an important parameter to consider when fitting the model spectra. A wide frequency band allows fitting of a large portion of the spectrum, which is consistent with the assumption that the entire eruption spectrum is produced by turbulence. Here, we identify 0.05–10 Hz as the frequency band containing the eruption signal, and note other bands may be relevant for other volcanoes and eruptions. We also restrict the peak frequency to be above 0.15 Hz, which assumes that the power of the turbulence spectrum is highest above that frequency. This cutoff distinguishes eruption signal from background noise that often has a similar slope, likely due to turbulence as a common source (Raspet & Webster, 2015). The selection of the frequency bandwidth and minimum peak frequency could be determined based on extended array processing methods that distinguish background noise from eruption signals in the future.

Overall the LST and FST model spectra fit the measured eruption spectrum very well for our examples, supporting the hypothesis that these eruptions produced a form of volcanic jet noise. Pre- and post-eruptive noise generally shows higher $RMSD$s than during the eruption across a large frequency band and

variations in the measured spectrum during an ongoing eruption are reflected in slight fluctuations of the $RMSD$. The observation of a change in the fit for certain frequencies is an important factor when determining the source of the sound and how eruption dynamics are reflected. We observe that the change in the misfit difference spectrogram during the eruptions coincides with a change in eruption dynamics.

Our findings encourage future quantitative investigations on the connection between eruption flow features, such as velocity, particle volume fraction, temperature of the erupting material (Matoza et al., 2013; McKee et al., 2017; Viswanathan, 2009), and erosion of the vent with volcano acoustic spectra. Laboratory experiments with controlled, particle-rich jets (e.g., Cigala et al., 2017) surrounded with microphones and cameras (Fernández et al., 2020) will inform how flow parameters affect the acoustic spectra. Additional consideration of numerical analysis as in Cerminara et al. (2016) and Taddeucci et al. (2014) will further refine the same mechanisms. The developed technique to fit a model spectra to data and quantitatively evaluate their fit has the potential to be used in other areas of research as well, for example, infrasonic conduit resonance or seismic tremor.

Data Availability Statement

The spectral fitting code can be found on github: https://github.com/jegestrich/simil_func including a script called example.py for a demonstration of the algorithm. The infrasound data recorded during the eruption of Kīlauea's fissure 8, Ahu'ailā'au, is publicly available at the IRIS DMC with network code 5L and station name FIS8 (at http://ds.iris.edu/mda/5L/), and data collection was facilitated by members of the U.S. Geological Survey's Hawaiian Volcano Observatory. The data from the MSH eruption are available through NRCan/CHIS autodrm tools (https://earthquakescanada.nrcan.gc.ca/stndon/AutoDRM/index-en.php) using the DC network code and station names MSH21, MSH22, MSH23, and MSH24. The Instituto Geofisico in Ecuador was immensely helpful in data collection, eruption observations, and engineering support at Tungurahua, and the data are available through NRCan/CHIS autodrm tools (https://earthquakescanada.nrcan.gc.ca/stndon/AutoDRM/index-en.php) using the DC network code and station name RIOE.

Acknowledgments
The authors acknowledge funding from NSF Grant EAR-1901614 and EAR-1847736. The majority of the study was done at the University of Alaska Fairbanks, located on the ancestral land of the Dena people of the lower Tanana River. We thank Jake Anderson, one anonymous reviewer and the Associated Editor for their helpful comments that improved the manuscript. Jörn Sesterhenn, Valeria Cigala, and Ulrich Kueppers provided helpful comments on volcanic jets.

References

Bishop, J. W., Fee, D., & Szuberla, C. A. L. (2020). Improved infrasound array processing with robust estimators. *Geophysical Journal International*, *221*(3), 2058–2074. https://doi.org/10.1093/GJI/GGAA110

Bowman, D. C., & Lees, J. M. (2017). A comparison of the ocean microbarom recorded on the ground and in the stratosphere. *Journal of Geophysical Research: Atmospheres*, *122*(18), 9773–9782. https://doi.org/10.1002/2017JD026474

Bowman, J. R., Baker, G. E., & Bahavar, M. (2005). Ambient infrasound noise. *Geophysical Research Letters*, *32*(9), 1–5. https://doi.org/10.1029/2005GL022486

Cerminara, M., Esposti Ongaro, T., & Neri, A. (2016). Large Eddy Simulation of gas–particle kinematic decoupling and turbulent entrainment in volcanic plumes. *Journal of Volcanology and Geothermal Research*, *326*, 143–171. https://doi.org/10.1016/j.jvolgeores.2016.06.018

Cigala, V., Kueppers, U., Peña Fernández, J. J., Taddeucci, J., Sesterhenn, J., & Dingwell, D. B. (2017). The dynamics of volcanic jets: Temporal evolution of particles exit velocity from shock-tube experiments. *Journal of Geophysical Research: Solid Earth*, *122*(8), 6031–6045. http://doi.wiley.com/10.1002/2017JB014149

Dabrowa, A. L., Green, D. N., Rust, A. C., & Phillips, J. C. (2011). A global study of volcanic infrasound characteristics and the potential for long-range monitoring. *Earth and Planetary Science Letters*, *310*(3–4), 369–379. https://doi.org/10.1016/j.epsl.2011.08.027

Delbos, F., Gilbert, J. C., Glowinski, R., & Sinoquet, D. (2006). Constrained optimization in seismic reflection tomography: A Gauss-Newton augmented Lagrangian approach. *Geophysical Journal International*, *164*(3), 670–684. https://doi.org/10.1111/j.1365-246X.2005.02729.x

Donn, W. L., & Naini, B. (1973). Sea wave origin of microbaroms and microseisms. *Journal of Geophysical Research*, *78*(21), 4482–4488. https://doi.org/10.1029/jc078i021p04482

Fee, D., & Garcés, M. (2007). Infrasonic tremor in the diffraction zone. *Geophysical Research Letters*, *34*(16), 1–5. https://doi.org/10.1029/2007GL030616

Fee, D., Garces, M., & Steffke, A. (2010). Infrasound from Tungurahua Volcano 2006-2008: Strombolian to Plinian eruptive activity. *Journal of Volcanology and Geothermal Research*, *193*(1–2), 67–81. https://doi.org/10.1016/j.jvolgeores.2010.03.006

Fee, D., & Matoza, R. S. (2013). An overview of volcano infrasound: From Hawaiian to Plinian, local to global. *Journal of Volcanology and Geothermal Research*, *249*, 123–139. https://doi.org/10.1016/j.jvolgeores.2012.09.002

Fernández, J. J. P., Cigala, V., Kueppers, U., & Sesterhenn, J. (2020). Acoustic analysis of starting jets in an anechoic chamber: Implications for volcano monitoring. *Scientific Reports*, *1–12*. https://doi.org/10.1038/s41598-020-69949-1

Ferrick, M. G., Qamar, A., & St. Lawrence, W. F. (1982). Source mechanism of volcanic tremor. *Journal of Geophysical Research*, *87*(B10), 8675. http://doi.wiley.com/10.1029/JB087iB10p08675

Foresee, F. D., & Hagan, M. T. (1997). Gauss-Newton approximation to Bayesian learning. *Proceedings of the 1997 International Joint Conference on Neural Networks*, *3*, 1930–1935. https://doi.org/10.1109/ICNN.1997.614194

Garcés, M., Fee, D., Steffke, A., McCormack, D., Servranckx, R., Bass, H., et al. (2008). Capturing the acoustic fingerprint of stratospheric ash injection. *Eos, Transactions American Geophysical Union*, *89*(40), 377–378. https://doi.org/10.1029/2008EO400001

Genco, R., Ripepe, M., Marchetti, E., Bonadonna, C., & Biass, S. (2014). Acoustic wavefield and Mach wave radiation of flashing arcs in Strombolian explosion measured by image luminance. *Geophysical Research Letters*, *41*, 7135–7142. https://doi.org/10.1002/2014GL061597

Gestrich, J. E., Fee, D., Tsai, V. C., Haney, M., & Van Eaton, A. R. (2020). A physical model for volcanic eruption tremor. *Journal of Geophysical Research: Solid Earth*, *125*, 1–28. https://doi.org/10.1029/2019jb018980

Hall, M. L., Steele, A. L., Mothes, P. A., & Ruiz, M. C. (2013). Pyroclastic density currents (PDC) of the 16-17 august 2006 eruptions of Tungurahua volcano, Ecuador: Geophysical registry and characteristics. *Journal of Volcanology and Geothermal Research*, *265*, 78–93. https://doi.org/10.1016/j.jvolgeores.2013.08.011

Harker, B. M., Gee, K. L., Neilsen, T. B., Wall, A. T., McInerny, S. A., & James, M. M. (2013). On autocorrelation analysis of jet noise. *Journal of the Acoustical Society of America*, *133*(6), EL458–EL464. https://doi.org/10.1121/1.4802913

Hedlin, M. A., Walker, K., Drob, D. P., & De Groot-Hedlin, C. D. (2012). Infrasound: Connecting the solid earth, oceans, and atmosphere. *Annual Review of Earth and Planetary Sciences*, *40*, 327–354. https://doi.org/10.1146/annurev-earth-042711-105508

Hupe, P., Ceranna, L., Pilger, C., De Carlo, M., Le Pichon, A., Kaifler, B., & Rapp, M. (2019). Assessing middle atmosphere weather models using infrasound detections from microbaroms. *Geophysical Journal International*, *216*(3), 1761–1767. https://doi.org/10.1093/gji/ggy520

Julian, B. R. (1994). Volcanic tremor: Nonlinear excitation by fluid flow. *Journal of Geophysical Research: Solid Earth*, *99*(B6), 11859–11877. http://doi.wiley.com/10.1029/93JB03129

Kanasewich, E. R., & Chiu, S. K. L. (1985). Least-squares inversion of spatial seismic refraction data. *Bulletin of the Seismological Society of America*, *75*(3), 865–880. https://doi.org/10.1785/BSSA0750030865

Kandula, M. (2008). On the scaling laws and similarity spectra for jet noise in subsonic and supersonic flow. *International Journal of Acoustics and Vibrations*, *13*(1), 3–16. https://doi.org/10.20855/ijav.2008.13.1220

Kieffer, S. W., & Sturtevant, B. (1984). Laboratory studies of volcanic jets. *Journal of Geophysical Research*, *89*(B10), 8253–8268. https://doi.org/10.1029/JB089iB10p08253

Lighthill, M. J. (1954). On sound generated aerodynamically II. Turbulence as a source of sound. *Proceedings of the Royal Society of London. Series A. Mathematical and Physical Sciences*, *222*(1148), 1–32. https://doi.org/10.1098/rspa.1954.0049

Lyons, J. J., Dietterich, H. R., Patrick, M. P., & Fee, D. (2021). High-speed lava flow infrasound from Kīlauea's fissure 8 and its utility in monitoring effusion rate. *Bulletin of Volcanology*, *83*(66), https://doi.org/10.1007/s00445-021-01488-7

Matoza, R. S., Fee, D., Garcés, M. A., Seiner, J. M., Ramón, P. A., & Hedlin, M. A. (2009). Infrasonic jet noise from volcanic eruptions. *Geophysical Research Letters*, *36*(8), 2–6. https://doi.org/10.1029/2008GL036486

Matoza, R. S., Fee, D., Neilsen, T. B., Gee, K. L., & Ogden, D. E. (2013). Aeroacoustics of volcanic jets: Acoustic power estimation and jet velocity dependence. *Journal of Geophysical Research: Solid Earth*, *118*(12), 6269–6284. https://doi.org/10.1002/2013JB010303

Matoza, R. S., Hedlin, M. A. H., & Garcés, M. A. (2007). An infrasound array study of Mount St. Helens. *Journal of Volcanology and Geothermal Research*, *160*(3–4), 249–262. https://doi.org/10.1016/j.jvolgeores.2006.10.006

McKee, K., Fee, D., Yokoo, A., Matoza, R. S., & Kim, K. (2017). Analysis of gas jetting and fumarole acoustics at Aso Volcano, Japan. *Journal of Volcanology and Geothermal Research*, *340*, 16–29. https://doi.org/10.1016/j.jvolgeores.2017.03.029

Neal, C. A., Brantley, S. R., Antolik, L., Babb, J. L., Burgess, M., Calles, K., et al. (2019). The 2018 rift eruption and summit collapse of Klauea Volcano. *Science*, *363*, 367–374. https://doi.org/10.1126/science.aav7046

Neilsen, T. B., Gee, K. L., Wall, A. T., James, M. M., & Atchley, A. A. (2013). Comparison of supersonic full-scale and laboratory-scale jet data and the similarity spectra for turbulent mixing noise. *Proceedings of Meetings on Acoustics*, *19*(040071), https://doi.org/10.1121/1.4799664

Oertel, H. (2004). *Prandtl's essentials of fluid mechanics*. *Applied Mathematical Sciences* (2nd ed.). Springer. https://doi.org/10.1007/b97538

Olson, J. V., & Szuberla, C. A. L. (2005). Distribution of wave packet sizes in microbarom wave trains observed in Alaska. *Journal of the Acoustical Society of America*, *117*(3), 1032–1037. https://doi.org/10.1121/1.1854651

Patrick, M. R., Dietterich, H. R., Lyons, J. J., Diefenbach, A. K., Parcheta, C., Anderson, K. R., et al. (2019). Cyclic lava effusion during the 2018 eruption of Kilauea Volcano. *Science*, *366*, 1213. https://doi.org/10.1126/science.aay9070

Peng, S., Lin, P., Du, W., & Lu, Y. (2017). The trust region method for time-domain full waveform inversion. In Q. Di, G. Xue, & J. Xia (Eds.), *Technology and application of environmental and engineering geophysics*. https://doi.org/10.1007/978-981-10-3244-8

Raspet, R., & Webster, J. (2015). Wind noise under a pine tree canopy. *Journal of the Acoustical Society of America*, *137*(2), 651–659. https://doi.org/10.1121/1.490658710.1121/1.4906587

Steffke, A. M., Fee, D., Garces, M., & Harris, A. (2010). Eruption chronologies, plume heights and eruption styles at Tungurahua Volcano: Integrating remote sensing techniques and infrasound. *Journal of Volcanology and Geothermal Research*, *193*(3–4), 143–160. https://doi.org/10.1016/j.jvolgeores.2010.03.004

Taddeucci, J., Sesterhenn, J., Scarlato, P., Stampka, K., Del Bello, E., Pena Fernandez, J. J., & Gaudin, D. (2014). High-speed imaging, acoustic features, and aeroacoustic computations of jet noise from Strombolian (and Vulcanian) explosions. *Geophysical Research Letters*, *41*(9), 3096–3102. https://doi.org/10.1002/2014GL061184

Tam, C. K. W. (2019). A phenomenological approach to jet noise: The two-source model. *Philosophical Transactions. Series A, Mathematical, Physical, and Engineering Sciences*, *377*(2159), 20190078. https://doi.org/10.1098/rsta.2019.0078

Tam, C. K. W., & Burton, D. E. (1984a). Sound generated by instability waves of supersonic flows. Part 1. Two-dimensional mixing layers. *Journal of Fluid Mechanics*, *138*, 249–271. https://doi.org/10.1017/S0022112084000112

Tam, C. K. W., & Burton, D. E. (1984b). Sound generated by instability waves of supersonic flows. Part 2. Axisymmetric jets. *Journal of Fluid Mechanics*, *138*, 273–295. https://doi.org/10.1017/S0022112084000124

Tam, C. K. W., Golebiowski, M., & Seiner, J. M. (1996). On the two components of turbulent mixing noise from supersonic jets. *American Institute of Aeronautics and Astronautics, Aeroacoustics Conference*. 1716. https://doi.org/10.2514/6.1996-1716

Viswanathan, K. (2009). Mechanisms of jet noise generation: Classical theories and recent developments. *International Journal of Aeroacoustics*, *8*(4), 355–407. https://doi.org/10.1260/147547209787548949

Watson, L. M., Dunham, E. M., & Johnson, J. B. (2019). Simulation and inversion of harmonic infrasound from open-vent volcanoes using an efficient quasi-1D crater model. *Journal of Volcanology and Geothermal Research*, *380*, 64–79. https://doi.org/10.1016/j.jvolgeores.2019.05.007

Waxler, R., & Gilbert, K. E. (2006). The radiation of atmospheric microbaroms by ocean waves. *Journal of the Acoustical Society of America*, *119*(5), 2651–2664. https://doi.org/10.1121/1.2191607

Welch, P. D. (1977). The use of fast Fourier Transform for the estimation of power spectra: A method based on time averaging over short, modified periodograms. *IEEE Transactions on Audio and Electroacoustics*, *15*(2), 70–73. https://doi.org/10.1109/TAU.1967.1161901

Wilson, L. (1976). Explosive volcanic eruptions—III. Plinian eruption columns. *Geophysical Journal International*, *45*(3), 543–556. https://academic.oup.com/gji/article-lookup/doi/10.1111/j.1365-246X.1976.tb06909.x

Woulff, G., & McGetchin, T. R. (1976). *Acoustic noise from volcanoes*.

Wright, S. J., & Nocedal, J. (2006). *Numerical optimization. Springer Series in Operations Research and Financial Engineering* (2nd ed.). Springer. https://doi.org/10.1007/978-0-387-40065-5

Reference From the Supporting Information

Tam, C. K. W., & Zaman, K. B. M. Q. (2000). Subsonic jet noise from nonaxisymmetric and tabbed nozzles. *AIAA Journal*, *38*(4), 592–599. https://doi.org/10.2514/2.1029